JGR Space Physics

RESEARCH ARTICLE
10.1029/2020JA027887

Special Section:
Probing the Magnetosphere through Magnetoseismology and Ultra-Low-Frequency Waves

Inner Magnetospheric ULF Waves: The Occurrence and Distribution of Broadband and Discrete Wave Activity

K. R. Murphy[1,2], A. R. Inglis[2,3], D. G. Sibeck[2], C. E. J. Watt[4], and I. J. Rae[5]

[1]Department of Astronomy, University of Maryland, College Park, MD, USA, [2]NASA Goddard Space Flight Centre, Greenbelt, MD, USA, [3]Department of Physics, Catholic University of America, Washington, DC, USA, [4]Department of Meteorology, University of Reading, Reading, UK, [5]Department of Space and Climate Physics, Mullard Space Science Laboratory, University College London, London, UK

Abstract Ultralow frequency (ULF) waves are electromagnetic pulsations observed throughout the magnetosphere driven by processes both external and internal to the magnetosphere. Within the magnetosphere, discrete and broadband ULF wave activity can couple to the local plasma via coherent or stochastic wave-particle interactions. These wave-particle interactions can lead to dynamic changes in local plasma including rapid acceleration and transport of radiation belt electrons. Using observations from GOES-15 and the Automated Flare Inference of Oscillations algorithm we investigate the distribution and occurrence of broadband and discrete ULF waves to help understand the relative importance of coherent and stochastic wave-particle interactions. We find that intervals of discrete ULF waves are more commonly identified during slow and low-density solar wind and when B_z is near zero. Broadband waves are more commonly identified during periods of active solar wind, including periods of high solar wind speeds and large density perturbations, and large negative B_z. We also find that under all solar wind conditions the number of intervals of broadband ULF wave power exceeds that of discrete wave power; for example, ULF wave activity is more likely to be broadband. These results suggest that radial diffusion due to incoherent broadband waves is an important driver of wave-particle interactions, especially during active solar wind conditions. However, the presence of discrete waves during both active and quiet solar wind conditions suggests that these waves and the corresponding wave-particle interactions cannot be ignored, especially since discrete wave-particle interactions tend to be more efficient than radial diffusion.

Key Points:
- The occurrence of discrete and broadband ULF waves is investigated using the Automated Flare Inference of Oscillations (AFINO) algorithm
- Discrete waves are more likely to occur during quiet solar wind and broadband during active solar wind conditions
- Our results suggest that radial diffusion and discrete wave-particle interactions are important in electron dynamics

Supporting Information:
- Supporting Information S1

Correspondence to:
K. R. Murphy,
kylemurphy.spacephys@gmail.com

Citation:
Murphy, K. R., Inglis, A. R., Sibeck, D. G., Watt, C. E. J., & Rae, I. J. (2020). Inner magnetospheric ULF waves: The occurrence and distribution of broadband and discrete wave activity. *Journal of Geophysical Research: Space Physics*, *125*, e2020JA027887. https://doi.org/10.1029/2020JA027887

Received 5 FEB 2020
Accepted 9 JUL 2020
Accepted article online 10 AUG 2020

1. Introduction

Electromagnetic waves and pulsations are fundamental features of the solar wind (e.g., Belcher & Davis, 1971; Smith et al., 1995; Tsurutani et al., 1994), magnetosphere (e.g., Jacobs et al., 1964; Menk, 2011), ionosphere (e.g., Hughes, 1974; Menk & Waters, 2013), and more broadly the solar system as a whole (e.g., Inglis et al., 2015; Kivelson, 2006). Of particular interest within the Earth's magnetosphere are ultralow frequency (ULF) wave pulsations in the Pc3–5 range (10–600 s, Jacobs et al., 1964); these waves are an important mechanism by which energy transfer can occur between the solar wind and the magnetosphere. Numerous physical mechanisms give rise to ULF wave structures in the Earth's magnetosphere, including Kelvin-Helmholtz instabilities (KHIs) (e.g., Mills & Wright, 1999; Southwood, 1968), pressure pulses in the solar wind (e.g., Kepko et al., 2002; Takahashi & Ukhorskiy, 2007), ion cyclotron waves in the foreshock (e.g., Eastwood et al., 2005; Hartinger et al., 2013), magnetospheric substorms (e.g., Olson, 1999; Rae & Watt, 2016; Volwerk, 2016), and unstable plasma distributions (e.g., Ozeke & Mann, 2001; Southwood et al., 1969). ULF waves can also couple to various plasma populations in the Earth's magnetosphere including the outer radiation belt and ring current, driving loss, energization, and transport of energetic electrons and ions (e.g., Horne & Thorne, 1998; Schulz & Lanzerotti, 1974; Thorne, 2010).

The coupling of ULF waves with energetic particles occurs as a result of wave-particle interactions whereby a ULF wave couples to the azimuthal drift motion of a charged particle resulting in the breaking of the third adiabatic invariant. This can occur via a resonant (e.g., Claudepierre et al., 2013) or diffusive (e.g., Schulz & Lanzerotti, 1974) process. In the resonant interaction, a monochromatic or discrete ULF wave with the appropriate mode structure and spectral characteristics can exchange energy with ions or electrons of a specific energy through the drift (e.g., Elkington et al., 1999, 2003) or drift-bounce (e.g., Ozeke & Mann, 2008;

Yeoman & Wright, 2001) mechanisms. In the diffusive interaction, a superposition of ULF waves, characteristic of broadband wave power, interacts stochastically with the local plasma via the drift resonance. The net result of this diffusive interaction, referred to as ULF radial diffusion, depends on the local phase space density gradient of the plasma and the varying spectral characteristics of the broadband ULF wave power such as amplitude and wave number (e.g., Fei et al., 2006; Olifer et al., 2019; Ozeke et al., 2014). A positive-phase space density gradient leads to a net inward transport and acceleration of plasma, and a negative-phase space density gradient leads to a net outward transport and de-energization of plasma. Since ULF radial diffusion is a stochastic process the overall wave-particle interaction is thought to be less efficient than discrete ULF wave resonances (e.g., Degeling et al., 2008; Elkington et al., 2003).

ULF waves were first reported in conjunction with a large geomagnetic storm and auroral activity observed between 28 August and 7 September 1859 (Stewart, 1861). Since then an extensive body of observational and theoretical work has been established regarding the generation, spectral, spatial, and temporal characteristics of these waves (see the reviews by Elkington, 2006; Menk, 2011; Plaschke, 2016; Rae & Watt, 2016; Takahashi, 2016; Volwerk, 2016). For example it has been demonstrated that ULF wave power is enhanced during elevated solar wind conditions (e.g., Anderson, 1994; Bentley et al., 2019; Murphy et al., 2011; Pahud et al., 2009; Rae et al., 2012; Takahashi & Ukhorskiy, 2007) and enhanced geomagnetic activity (e.g., Brautigam et al., 2005; Hartinger et al., 2015; Ozeke et al., 2014). These intervals of elevated ULF wave power can manifest as localized field line resonances (FLRs) (e.g., Mann et al., 2002; Rae et al., 2005), broadband-driven FLRs that can exhibit multiple harmonics at a fixed location or a spectrum of resonances throughout the magnetosphere (e.g., Hasegawa et al., 1983; Takahashi & McPherron, 1982, 1984; Wharton et al., 2019), as well as enhanced broadband wave power (e.g., Murphy et al., 2011; Sarris, 2014). It has also been demonstrated, in both case and statistical studies, that these periods of enhanced ULF wave power are strongly related to the dynamics of energetic electrons in the outer radiation belt (e.g., Mann et al., 2013; Mathie & Mann, 2001; Murphy et al., 2020; O'Brien et al., 2001; Olifer et al., 2019). However, the conditions that preferentially give rise to either discrete or broadband ULF wave power within the Earth's magnetosphere have not been comprehensively investigated. This includes whether there are preferential locations for increased discrete or broadband wave activity; whether these locations change during quiet (e.g., slow/low-density solar wind and B_z near 0) and active (e.g., high-speed solar wind and large negative B_z) solar wind intervals; and whether there are differences in the mode structure and period of discrete ULF waves at different magnetospheric locations. Understanding the occurrence and characteristics of both broadband and discrete ULF waves in the Earth's magnetosphere is fundamental to understanding and accurately quantifying ULF wave-particle interactions and determining whether the process is predominantly mediated by radial diffusion or discrete resonance (e.g., Murphy et al., 2018).

This work systematically surveys GOES magnetometer data, adopting the novel Automated Flare Inference of Oscillations (AFINO) technique (e.g., Inglis et al., 2015, 2016) to identify intervals of either discrete or broadband ULF wave activity. Using results from AFINO we explore the dependence of discrete and broadband ULF wave activity on magnetic local time (MLT) and the physical properties of the solar wind. In this manuscript section 2 describes the data and methodology used to identify discrete and broadband ULF wave activity. Section 3 presents the results, comparing the occurrence of discrete and broadband ULF waves, and investigates the period of discrete ULF waves as a function of MLT, wave mode, and the local magnetic field and IMF strength. Section 4 discusses the results from section 3 and provides a brief conclusion. In general we find that discrete ULF wave activity can account for as much as one third of all activity (discrete and broadband) and is most likely to occur during quiet solar wind conditions when the solar wind speed and density is low and IMF B_Z is near zero. Conversely, broadband wave activity peaks during active solar wind conditions where the solar wind velocity is high, when there are large perturbations in the solar wind density, and when the IMF B_Z is increasingly negative. These results suggest that both discrete and diffusive wave-particle interactions can be important in radiation belt dynamics under varying solar wind activity.

2. Data Selection and Analysis Methods

2.1. GOES Magnetometer Data

The Geostationary Operational Environment Satellite (GOES) series of East and West spacecraft have provided high-fidelity observations of the Earth's magnetic field at geosynchronous orbit for over three decades. The more recent GOES N, O, and P series spacecraft (GOES-NOP for short) are equipped with two flux-gate

magnetometers, an inboard and an outboard, which measure the magnetic field in three perpendicular components at a constant cadence of 0.512 s (e.g., Singer et al., 1996). This provides an extensive data set at 6.6 R_E with which to characterize Earth's magnetic field. In this study, we analyze 4 years of continuous GOES-NOP series magnetic field observations from the GOES-15 outboard magnetometer, during a portion of the Van Allen Probes era (2013–2016) (Mauk et al., 2013) to characterize the occurrence of discrete and broadband ULF pulsations of the Earth's magnetic field.

Both GOES-15 magnetometers provide measurements of three perpendicular components of the in situ magnetic field, denoted H_E, H_P, and H_N. In this coordinate system, H_E lies parallel to the satellite-Earth line, pointing earthward, and hence lies close to the equatorial plane. H_P is aligned with spacecraft orbit normal, closely aligned with Earth's spin axis, while H_N is perpendicular to H_E and H_P pointing eastward. In this study we use the outboard magnetometer with AFINO, while the inboard magnetometer is used in conjunction with the outboard magnetometer to help identify periods of poor data quality. We focus on observations from GOES-15, corresponding to GOES West (until December 2018 when GOES-17 took over), which lies closest to the Earth's magnetic equator such that in the *EPN* coordinate system, compressional waves are primarily observed in the H_P component, poloidal waves in the H_E component, and toroidal wave modes are associated with the H_N component. In a statistical study the *EPN* coordinate system has the benefit that it is fixed and always well defined. Conversely, in a statistical study, it is difficult to produce a well-defined and robust field-aligned coordinate system as impulsive and large-amplitude field changes will ruin any field-aligned coordinate transformation; this is especially true on the nightside. In addition, the GOES onboard heater introduces a step change in the magnetometer time series every time it is turned on or off (see section 2.3). When this occurs the quality of data is degraded, and the data are discarded. These step changes are observed frequently in the GOES H_N magnetic field component and lead to over half of the H_N data being discarded from the study. In the H_P and H_E magnetic field components these step changes are smaller and lead to less than 5% of intervals being discarded (see the supporting information for additional details). Because of these step-like changes any field-aligned coordinate transform will result in a significant increase in discarded data by rotating the discontinuity produced by the heaters into all three magnetic field components, as opposed to a single magnetic field component. Hence for the purpose of this study we have chosen to utilize the fixed and well-defined GOES *EPN* coordinate system. Finally, it is important to note that the relation between the *EPN* coordinate system and compressional, poloidal, and toroidal waves is specific to spacecraft whose orbits are close to the equatorial plane.

In addition to GOES magnetometer data, near-Earth solar wind measurements from the OMNIWeb database are used to study the relation between the solar wind and discrete and broadband ULF wave pulsations. Here we utilize the 1 min high-resolution OMNI data set providing measurements of the solar wind composed of multiple physical parameters including speed, density, and magnetic field. These data are taken from measurements made by multiple spacecraft including ACE (Stone et al., 1998) and WIND (Lepping et al., 1995), both of which are in a near-L1 orbit. These data sets are amalgamated and time shifted to correspond to the solar wind properties at the estimated position of the bow shock nose, providing a single, continuous data set (King & Papitashvili, 2005).

2.2. The AFINO Code

To investigate the occurrence of discrete and broadband ULF wave power in the inner magnetosphere we utilize the AFINO code (Inglis et al., 2015, 2016). AFINO was developed as a tool to systematically identify quasiperiodic pulsations in a large number of solar flares. It was one of a suite of techniques blind tested by Broomhall et al. (2019), who investigated the performance of different oscillation detection methods on controlled, simulated data sets. Broomhall et al. (2019) found that AFINO was a robust method for identifying quasiperiodic pulsations and characterizing the dominant frequency of the pulsations with a particularly low rate of false positives. The AFINO code was developed so that it could be straightforwardly adapted to operate on a variety of temporal series, including magnetospheric data. This was recently demonstrated by Murphy et al. (2018), who used AFINO to identify and characterize the frequency, amplitude, and azimuthal wave number of discrete ULF waves during a geomagnetic storm observed by the Magnetospheric Multiscale Mission. In this study we utilize AFINO as it systematically characterizes a time series as either broadband or discrete based on a goodness of fit to modeled broadband and discrete spectra with a low rate of false positives (Broomhall et al., 2019). This provides a robust and quantifiable definition of the type of ULF wave

allowing for the statistical study of the occurrence of both broadband and discrete ULF wave power within the magnetosphere.

For a given time series, AFINO operates by examining the Fourier power spectrum of the series. Using a data-model comparison, AFINO determines the best representation of the time series' power spectra. In this way AFINO can separate intervals of broadband power from intervals where a frequency enhancement or discrete wave was present. The AFINO method is described in detail by Inglis et al. (2015, 2016), as well as by Murphy et al. (2018). Therefore, in this work, we limit ourselves to summarizing the key steps in algorithm as follows:

1. Normalize the input time series by subtracting and then dividing by the time series average and apply a Hanning window. The normalization is for convenience only, while the Hanning window mitigates the effects of finite-duration time series on the calculation of the Fourier power spectrum.
2. Calculate the Fourier power spectrum defined here as $P = abs(FFT\ (G_{ts}))^2$, where P is the power, FFT is the fast Fourier transform, and G_{ts} is the GOES time series.
3. Fit a suite of spectral models to the Fourier power spectrum using a maximum likelihood estimation method. Here we consider three models: a single power law (S_0), a power law with an additional localized enhancement (S_1), and a broken power law (S_2) (Equations 3–5).
4. Use the Bayesian information criterion (BIC) (Schwarz, 1978) to determine which of the models is the best representation of the data. The BIC is given by

$$BIC = -2\ln(L) + k\ln(n) \tag{1}$$

   where L is the maximum likelihood, k is the number of free parameters, and n is the number of data points in the analyzed power spectrum. The $k\ln(n)$ term effectively penalizes a model with additional free parameters, therefore testing whether additional complexity is justified.
5. Verify the fit quality of each model using the χ^2-like statistic for exponentially distributed data (Nita et al., 2014) (Equation 2) to determine whether any of the fitted models are appropriate, defined as

$$\chi^2_\nu = \frac{1}{\nu}\sum_{j=1}^{n}(1-\hat{\rho}_j)^2 \tag{2}$$

   which can be used to find the probability p of the data given the chosen model (see Nita et al., 2014, Appendix A). Models with outlying values of p (<0.05) are not considered appropriate representations of the data.
6. The best model is identified by calculating $\Delta BIC_{ij} = BIC_i - BIC_j$ for all combinations of models i and j. For a model to be considered over the others we require that it be strongly preferred by minimizing the BIC meeting the criteria that $\Delta BIC_{ij} > 10$ when compared to all other models (see, e.g., Burnham & Anderson, 2004; Raftery, 1995). It must also satisfy the conditions on the probability p described above.

In this work, we utilize the test models described by Inglis et al. (2015, 2016). The simplest model S_0 represents broadband power, which naturally arises in bursty time series (Cenko et al., 2010; Gruber et al., 2011; Huppenkothen et al., 2019; Huppenkothen et al., 2013; Ireland et al., 2015; Rae et al., 2012; Vaughan, 2005). The second model S_1 is equivalent to model S_0 plus an extra term corresponding to a Gaussian enhancement in log-frequency space. This model component is designed to represent a discrete wave signature, that is, an oscillation in a localized frequency range (e.g., Murphy et al., 2011). Model S_2 is an alternative broadband wave power hypothesis similar to model S_0, but with a spectral break, which can be observed in magnetic fluctuations separating various plasma scales (e.g., ions and electrons) (e.g., Chen et al., 2014). The potential for a spectral break allows broad features in the Fourier spectrum to be captured without resorting to an oscillation model. Formally, these three models may be written as

$$S_0(f) = A_0 f^{-\alpha_0} + C_0 \tag{3}$$

$$S_1(f) = A_1 f^{-\alpha_1} + B\ \exp\left(\frac{-(\ln f - \ln f_p)^2}{2\sigma^2}\right) + C_1 \tag{4}$$

$$S_2(f) = \begin{cases} A_2 f^{-\alpha_b} + C_2, & \text{if } f < f_{\text{break}} \\ A_2 f^{-\alpha_b-\alpha_a} f^{-\alpha_a} + C_2, & \text{if } f > f_{\text{break}} \end{cases} \tag{5}$$

for frequencies f, where A_x and B are amplitudes, α_x are power law indices, C_x are constants, and f_p and σ represent the location in frequency of a Gaussian peak and its width, respectively. Based on the steps outlined above, AFINO can analyze a time series—in this case the magnetic field data measured by GOES—and classify the time series as either a broadband or discrete time series depending on which model is strongly preferred.

2.3. Methodology

Throughout 2013–2016, AFINO is applied to each magnetic field component measured by GOES-15 in overlapping 1 hr intervals stepped every 20 min; this gives a total of 70 intervals each day for each component. Each interval is then characterized as either a broadband S_0 or S_2 or discrete wave S_1 signal. The overlapping windows ensure that localized times of discrete wave activity are not overlooked due to edge effects. An interval is defined as discrete when model S_1 is strongly preferred; if model S_1 is not strongly preferred but either model S_0 or S_2 satisfies the condition $p > 0.05$, the interval is classified as broadband, otherwise the interval is classified as a poor fit ($p_i < 0.05$) and discarded from the study. Each interval is also associated with the predominant hourly solar wind conditions. Finally, intervals of discrete wave power are assigned to one of the compressional, poloidal, or toroidal wave modes based on which of the H_P, H_E, and H_N components is dominant during that interval; that is, which has the largest overall amplitude. Note that for the purpose of this study, if a wave is observed in multiple components, the nondominant components are characterized as broadband power. This allows the dominant mode of each discrete wave to be identified and also avoids double or triple counting of a discrete wave when it is observed in two or three of the magnetic field components.

Figure 1 shows three examples of the AFINO analysis applied to GOES-15 H_E data. The original signals are shown in the left column, while the fits to models S_0 (single power law), S_1 (discrete wave signature), and S_2 (broken power law) are shown in the subsequent three columns. These examples show the different types of results obtained by AFINO. In the first example a broken power law is sufficient to describe the magnetometer data, and there is no evidence of discrete power. The second example shows the opposite, where model S_1 is strongly preferred over the others, showing the presence of a discrete wave with a characteristic period of ~135 s. Finally, the third example shows a more complex scenario; although the discrete power model S_1 is strongly preferred over the others, it does not fully describe the magnetometer data. This is illustrated by the p value for this model, which is less than 0.05, indicating a poor overall fit to the PSD. Examination of the PSD shows that this is due to the presence of multiple discrete frequencies in the magnetic field data. The S_1 model is unable to model all of these frequencies simultaneously, and the low p value for models S_0 and S_2 results in this interval being discarded from the study. An investigation of 1,000 random discarded time series demonstrates that few events are discarded from our study as result of multiple frequency peaks leading to poor fits; hence, even when multiple frequencies exist, AFINO is still able to identify a discrete peak and classify the interval as discrete. Though multiple frequencies can be common in ULF wave observations (e.g., Takahashi & Denton, 2007), this study focuses on the investigation of the relative occurrence of discrete and broadband intervals; thus, the occurrence of multiple frequencies does not affect the results nor the discussion and conclusions presented sections 3 and 4.

It is important to note that although the GOES-15 magnetometer data have a temporal resolution of 0.512 s, at times, the data can include high-frequency artifacts as a result of changes in the onboard heater system. When turned on or off the heaters cause small discontinuities in the time series of a few nanotesla. Though small, these discontinuities create harmonics within the Fourier spectra, which may be misidentified as intervals of discrete wave power. When comparing the time series from both the outboard and inboard GOES-15 magnetometers these discontinuities tend to be out of phase such that the correlation between two magnetometers tends to be small. Using a simple correlation threshold we are able to remove intervals containing a discontinuity arising from the heaters being turned on and off. In this study any interval with a correlation below 0.8 between the outboard and inboard magnetometers is removed from the overall analysis. Further, when the heater are on they generate identifiable harmonics or frequencies in the Fourier spectrum, typically limited to frequencies >1 Hz. For this reason, although the full-resolution data are used throughout this study, only frequencies <100 mHz are considered in the Fourier domain, with higher frequencies ignored. This allows for detection and characterization of discrete wave power with periods of 10 s or longer, sufficient for Pc3–5 ULF waves.

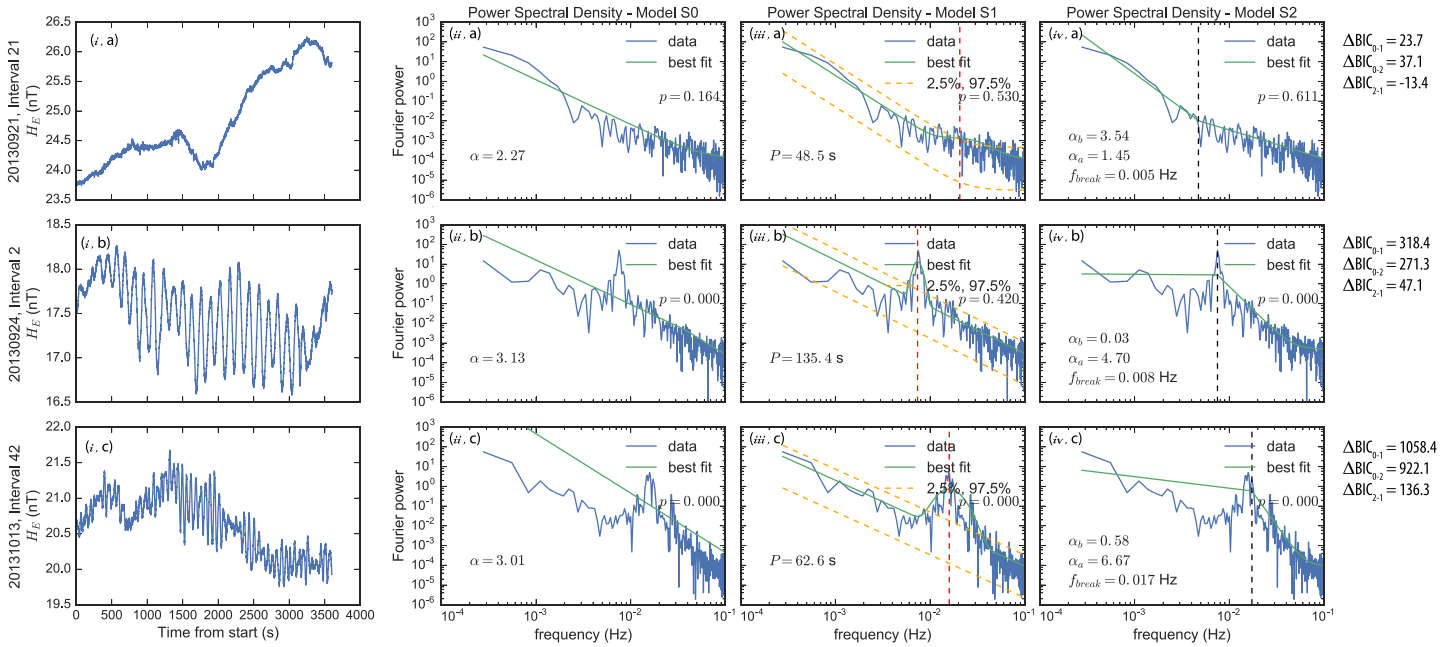

Figure 1. Examples of the AFINO code operating on GOES-15 magnetometer data. For each row (a–c), Column i shows the H_E component of the magnetic field as a function of time for a 1 hr interval. Columns i–iv show the best fits of the models S_0, S_1, and S_2 to the Fourier power of the series. (a) One hour interval from 21 September 2013, showing no evidence of discrete power—the broken power law model S_2 is preferred (a, iv). (b) An interval from 24 September 2013, showing a discrete wave detected by AFINO with a period of 135 s (b, iii). (c) An interval from 13 October 2013, showing a complex interval where none of the three models fully represent the data.

3. Results

In the following subsections we investigate the distribution of discrete and broadband intervals of ULF wave power as a function of magnetic field component, ULF wave band, and MLT; the relative occurrence of discrete and broadband waves as a function of MLT and solar wind activity; and the period of discrete ULF waves as a function of solar wind IMF and the local magnetic field.

3.1. Distribution of Discrete and Broadband ULF Wave Intervals

Figure 2 shows the polar histogram of discrete (gray) and broadband (blue) ULF wave intervals as a function of MLT and magnetic field component. The radial axis in each plot shows the number of counts in each MLT bin. Here, each 1 hr interval of discrete wave power is assigned to the compressional, poloidal,

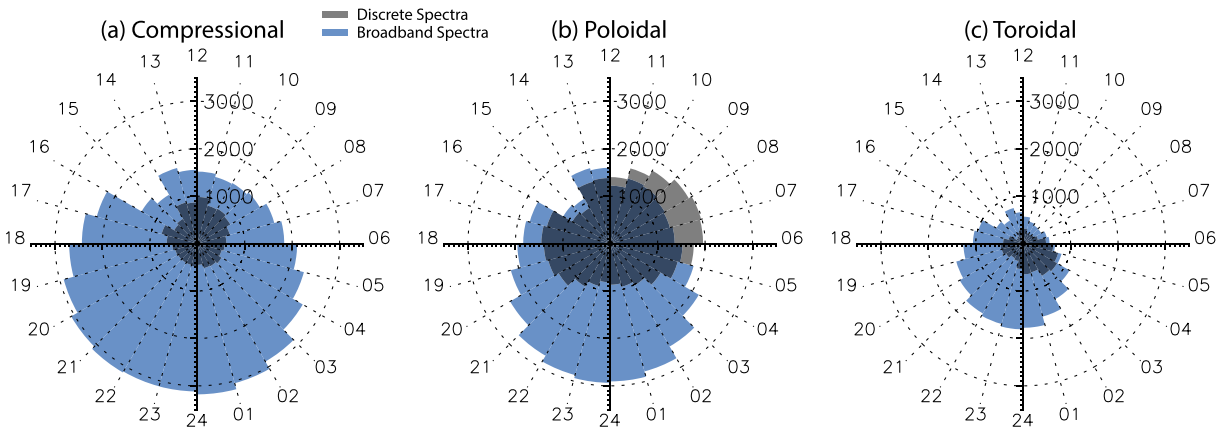

Figure 2. Polar histograms showing the occurrence of discrete and broadband ULF intervals as a function of MLT. The radial axis shows the number of counts in each MLT bin as a function of magnetic field component (top) and wave band (bottom). From left to right are the distributions of (a) compressional, (b) poloidal, and (c) toroidal magnetic field components; discrete and broadband intervals are shown by the gray and blue histograms, respectively.

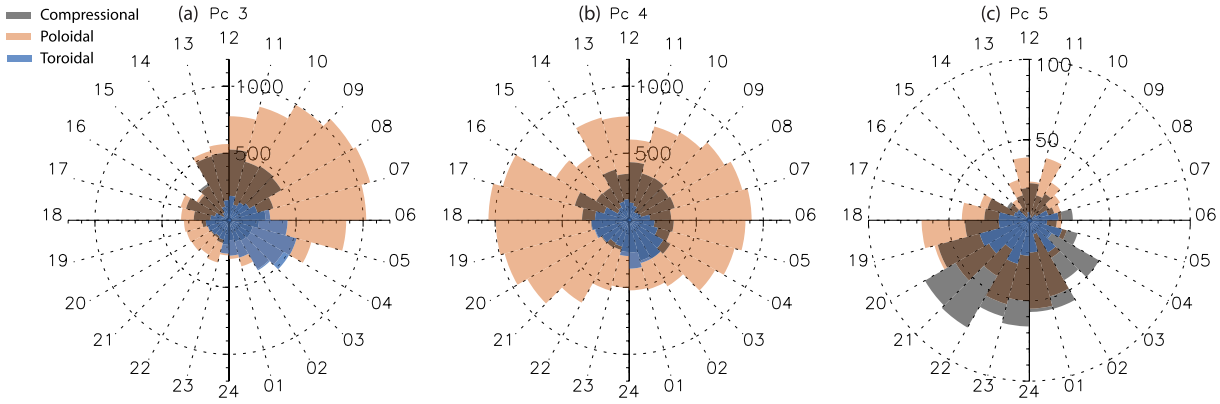

Figure 3. Polar histograms showing the occurrence of discrete waves in the Pc3, Pc4, and Pc5 wave bands for (a) compressional (gray), (b) poloidal (orange), and (c) toroidal (blue) wave modes.

or toroidal wave modes as described in section 2.3. The supporting information contains additional details on the distribution of intervals analyzed by the AFINO algorithm not presented here. This includes the full distribution of events discrete, broadband, or discarded, for each of the three magnetic field components. These distributions are further broken down into their constituent parts; for example, broadband intervals are broken into whether S_0 or S_2 is preferred, and discarded intervals are broken into bad data or poor fits (Figures S1–S3). A brief description of Figures S1–S3 is provided in Text S4.

As can be seen in Figure 2 the occurrence of broadband ULF wave power is higher than that of discrete ULF wave power in nearly all MLT sectors. The exception to this is the occurrence of discrete poloidal mode ULF wave power in the postdawn and prenoon sectors (05–12 MLT), which exceeds that of broadband wave power. Also evident in Figure 2 is that the occurrence of broadband ULF wave power peaks on the nightside (18–06 MLT) for all components, characteristic of substorm activity.

With regard to the occurrence of discrete ULF wave intervals the most apparent results from Figure 2a are a clear enhancement in the compressional component of discrete ULF waves throughout the dayside and peaking in the noon sector 08–13 MLT. In the poloidal component (Figure 2b), discrete ULF waves peak on the dawn flank between 06 and 11 MLT and again in the dusk sector between 16 and 21 MLT. The occurrence of discrete toroidal waves (Figure 2c) peaks in the postmidnight sector between 03 and 06 MLT, although the statistics are much lower for this mode. Potential generation mechanisms are discussed in detail in section 4.

Figure 3 shows the polar histograms of discrete waves as a function of MLT, wave mode, and ULF wave band. The radial axis indicates the number of events in each MLT bin. Here each interval of discrete wave power is divided into the appropriate ULF wave band (Jacobs et al., 1964) according to the dominant frequency of the wave identified by AFINO. As can be seen in Figure 3a discrete poloidal Pc3 waves (10–45 s) peak in the morning to early afternoon sector (05–12 MLT), compressional around noon (08–14 MLT), and toroidal waves in the postmidnight sector. Discrete Pc4 waves (45–150 s) (Figure 3b) are most prevalent in the poloidal component peaking on the dawn and dusk flanks, with compressional and toroidal waves occurring around noon and midnight, respectively. Discrete Pc5 waves (150–1,000 s) (Figure 3c) are most prominent on the nightside in all three magnetic field components. Also evident in Figure 3 is that significantly more discrete Pc3 and Pc4 waves are identified by AFINO then Pc5 waves. This may be a feature of the structure of FLRs in the magnetosphere combined with the implementation of the AFINO algorithm, which we elaborate in section 4.

3.2. Relative Occurrence of Discrete and Broadband ULF Wave Intervals

This section investigates the relative occurrence of broadband and discrete ULF wave intervals at geosynchronous orbit as a function of solar wind driving. Figure 4 shows the MLT distribution of discrete and broadband ULF wave intervals as well as the ratio of discrete to broadband occurrence as function of solar wind speed for each of the three magnetic field components. We investigate the occurrence of discrete and broadband wave power as a function of v_{sw} as several studies have shown that ULF wave amplitudes increase

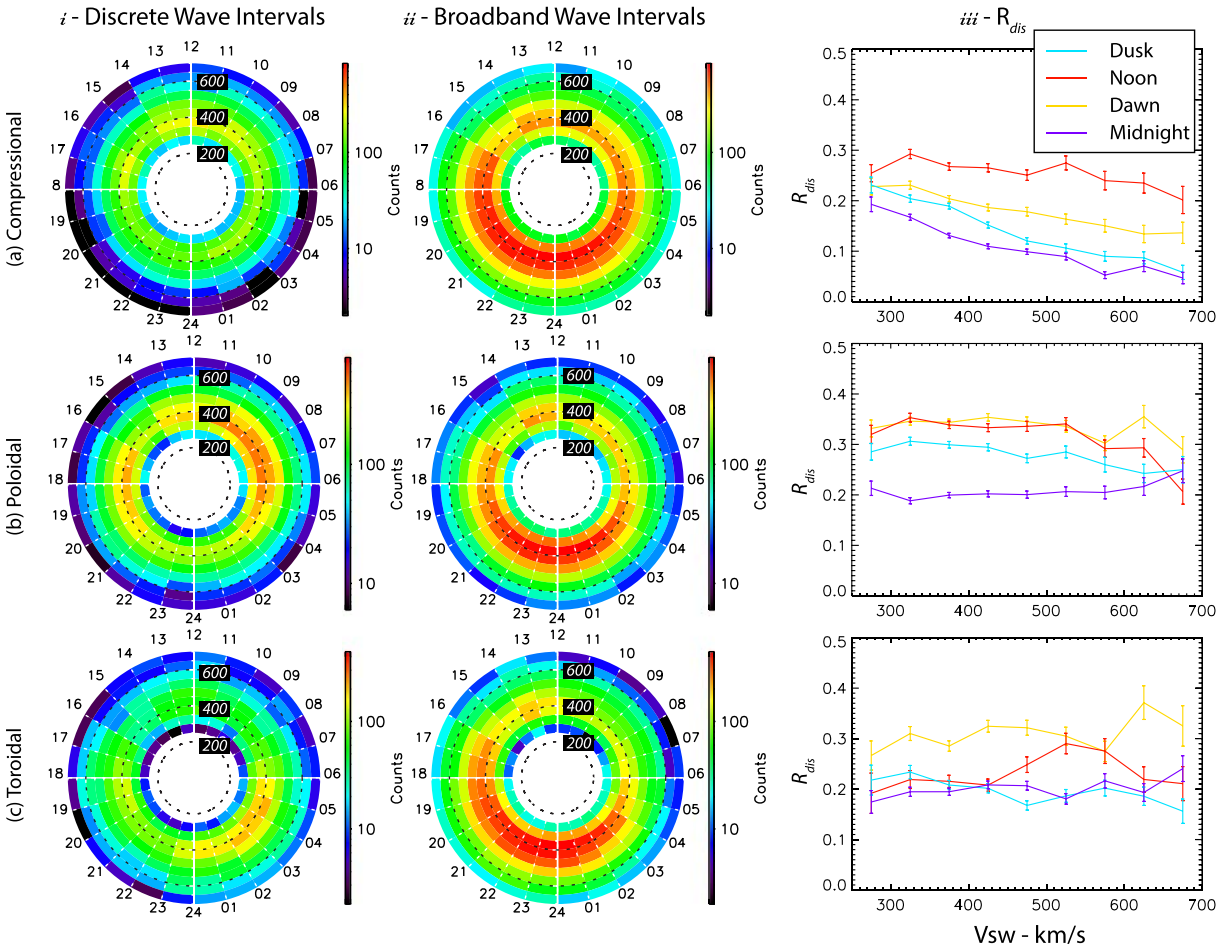

Figure 4. Dependence of the ratio between discrete and discrete plus broadband events, R_{dis}, on the solar wind velocity v_{sw}. (Column i) Polar histogram of the number of ULF discrete intervals identified by AFINO as a function of MLT (azimuth) and solar wind velocity (radial—km/s), for (a) compressional-dominant, (b) poloidal-dominant, and (c) toroidal-dominant intervals. (Column ii) Histogram of the number of broadband ULF wave intervals as a function of MLT and solar wind velocity. (Column iii) The ratio of the distribution of discrete to broadband ULF wave intervals as a function of solar wind speed (x axis) and MLT sector (color). In Column iii the four MLT sectors are dawn (03–09 MLT, yellow), noon (09–15 MLT, red), dusk (15–21 MLT, blue), and midnight (21–03 MLT, purple).

with increasing v_{sw} (e.g., Bentley et al., 2019; Mathie & Mann, 2001). Due to poor statistics we have not included the relative occurrence of broadband and discrete ULF wave intervals as a function of geomagnetic activity (e.g., *Dst*).

The first column of Figure 4 shows polar histograms of the number of discrete ULF wave intervals as a function of MLT and solar wind speed v_{sw} (radial axis). Similar to Figure 2, Figure 4a, i shows that the occurrence of discrete compressional ULF wave intervals peaks around noon. Discrete poloidal ULF wave intervals (Figure 4b, i) peak on the dawn and dusk flanks and toroidal ULF wave intervals (Figure 4c, i) in the postmidnight sector for moderate solar wind speeds between 300 and 500 km/s. Column ii shows the same polar histograms as Column i but for broadband intervals. In each of the three components broadband ULF wave intervals peak in the duskside and nightside magnetosphere for moderate to high solar wind speeds between 300 and 550 km/s.

Figure 4, iii illustrates the key feature of interest in this study, how the relative occurrence between discrete and broadband ULF wave intervals as characterized by AFINO varies as a function of MLT and solar wind speed v_{sw}. The ratio of discrete to the total number of events R_{dis} is defined as the number of discrete intervals (S_1) for a given solar wind and MLT bin $N_{dis}(v_{sw},MLT)$, divided by the total number of intervals N_T (discrete and broadband, $S_0+S_1+S_2$) in the same solar wind and MLT bin given by $N_T(v_{sw},MLT)=N_{dis}(v_{sw},MLT)+N_{bdb}(v_{sw},MLT)$, and $N_{bdb}(v_{sw},MLT)$ is the sum of S_0 and S_2 intervals for a

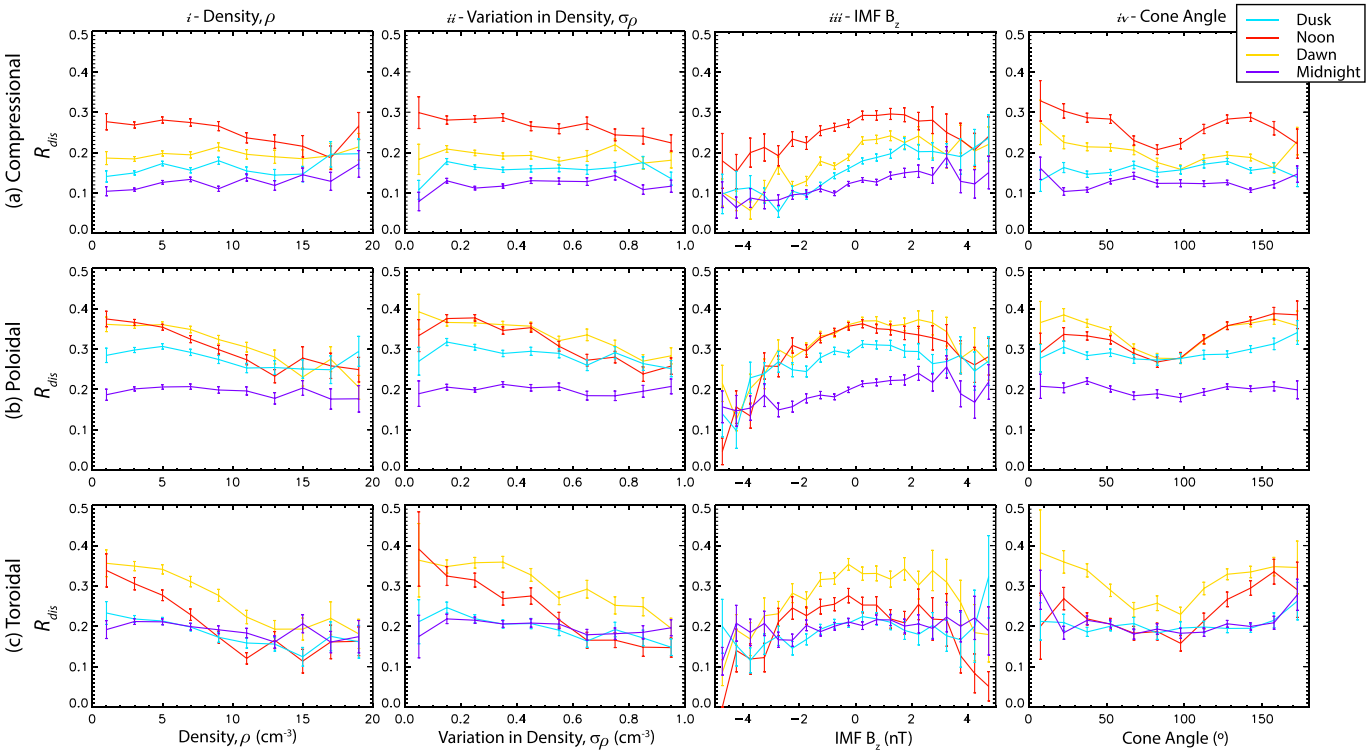

Figure 5. Ratio between the occurrence of discrete and broadband ULF wave intervals R_{dis} as a function of (i) solar density ρ, (ii) variation in solar wind density σ_ρ, (iii) IMF B_z, and (iv) IMF cone angle. Each column is in the same format as Figure 4, iii and shows the variation in R_{dis} as a function of MLT (color) and magnetic field component (a–c). The variation in solar wind density σ_ρ is calculated for each hourly interval by differencing the solar wind density time series and calculating the standard deviation of the resulting time series. In this way, hourly intervals where solar wind density rapidly varies will have a large σ_ρ. The IMF cone angle is defined as $\cos^{-1}(B_x/B)$.

given solar wind and MLT bin such that $R_{bdb} = 1 - R_{dis}$. Here, we separate ULF observations into four MLT sectors: dawn (03–09 MLT), noon (09–15 MLT), dusk (15–21 MLT), and midnight (21–03 MLT), to investigate the ratio of discrete to broadband wave events as a function of v_{sw} and MLT sector.

For the compressional and poloidal components, there is a decrease in R_{dis} as v_{sw} increases in the dawn, noon, and dusk sectors. In the midnight sector R_{dis} decreases with increasing v_{sw} in the compressional component and slightly increases with increasing v_{sw} in the poloidal component. In the toroidal magnetic field component R_{dis} shows no clear trend and tends to be quite variable in in the noon and dawn sectors and relatively flat in the dusk and midnight sectors. In the remainder of this section we explore how the ratio of discrete and broadband ULF wave intervals varies with MLT sector as a function of solar wind density and the variation in solar wind density σ_ρ, IMF B_z, and IMF cone angle.

Figure 5, i–iv shows the variation in R_{dis} the ratio of discrete to both discrete and broadband intervals as function of solar wind density ρ (proton number density), the variation in solar wind density σ_ρ, IMF B_z, and IMF cone angle in the same format as Figure 4, iii. The occurrence of discrete and broadband ULF wave power is studied with respect to these parameters as they have been shown to be linked to the generation (e.g., Bier et al., 2014; Hartinger et al., 2013) and amplitude (e.g., Bentley et al., 2019) of ULF waves in the magnetosphere. The trend in R_{dis} as a function of solar wind density ρ is mixed. For the compressional component (Figure 5a, i), there is evidence of a decrease in R_{dis} for increasing ρ in the noon sector, whereas in the dusk, dawn, and midnight sectors, R_{dis} remains relatively flat. For the poloidal and toroidal components (Figures 5b, i and 5c, i), R_{dis} decreases as density increases up to $\rho = 15$. At very high density values $\rho > 15$, there is evidence of an increase in discrete ULF wave events, particularly on the dawn flank. Apparent in Figure 5, ii is a decrease in R_{dis} during periods of high σ_ρ in all three magnetic field components in both the noon and morning sectors, although this effect is less pronounced for compressional mode ULF waves. In the dusk and midnight sectors there is no clear trend in R_{dis} as a function of σ_ρ.

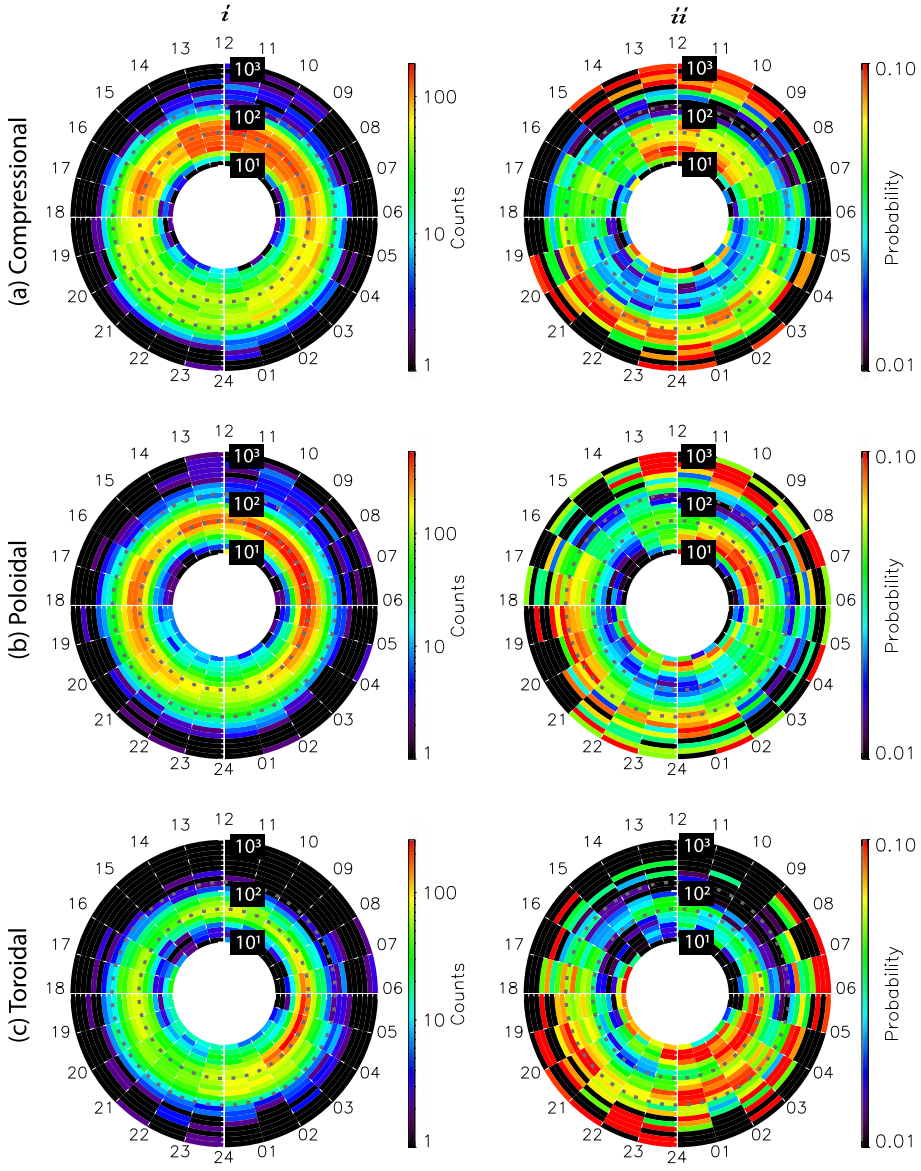

Figure 6. Two-dimensional (i) polar histograms and (ii) probability distributions of discrete ULF wave periods (radial axis) as a function of MLT (azimuthal axis) and magnetic field component (a–c). The probability distribution (ii) shows the probability of observing a specific period at a given MLT such that each shell (or radial bin) adds to 1. The dotted circles at 45 and 150 s mark the separation between the Pc3 and Pc4 wave bands and the Pc4 and Pc5 wave bands, respectively.

Figure 5, iii shows that relative to IMF B_z R_{dis} in each of the field components is largest when B_z is close to zero, or slightly positive and falls with increasingly positive or negative B_z in each MLT sector. Figure 5, iv shows the dependence of R_{dis} on the IMF cone angle, defined as $\cos^{-1}(Bx/B)$ such that when the IMF is directed on the Sun-Earth line, the cone angle is zero. For all three components, there is a dip in R_{dis} at 90° in the noon and dusk sectors, such that discrete ULF waves are less common when the IMF is predominantly in the x direction or perpendicular to the Sun-Earth line in the y-z plane. In the dusk and midnight sectors R_{dis} is generally constant as a function of cone angle.

3.3. Distribution of ULF Wave Periods

Figure 6 shows the two-dimensional statistical distributions of discrete ULF waves identified by AFINO as a function of wave period, MLT, and magnetic field component. The period for each interval of discrete wave power is determined from the model parameter f_p in model S_1 (section 2.2). The polar histograms in Figure 6,

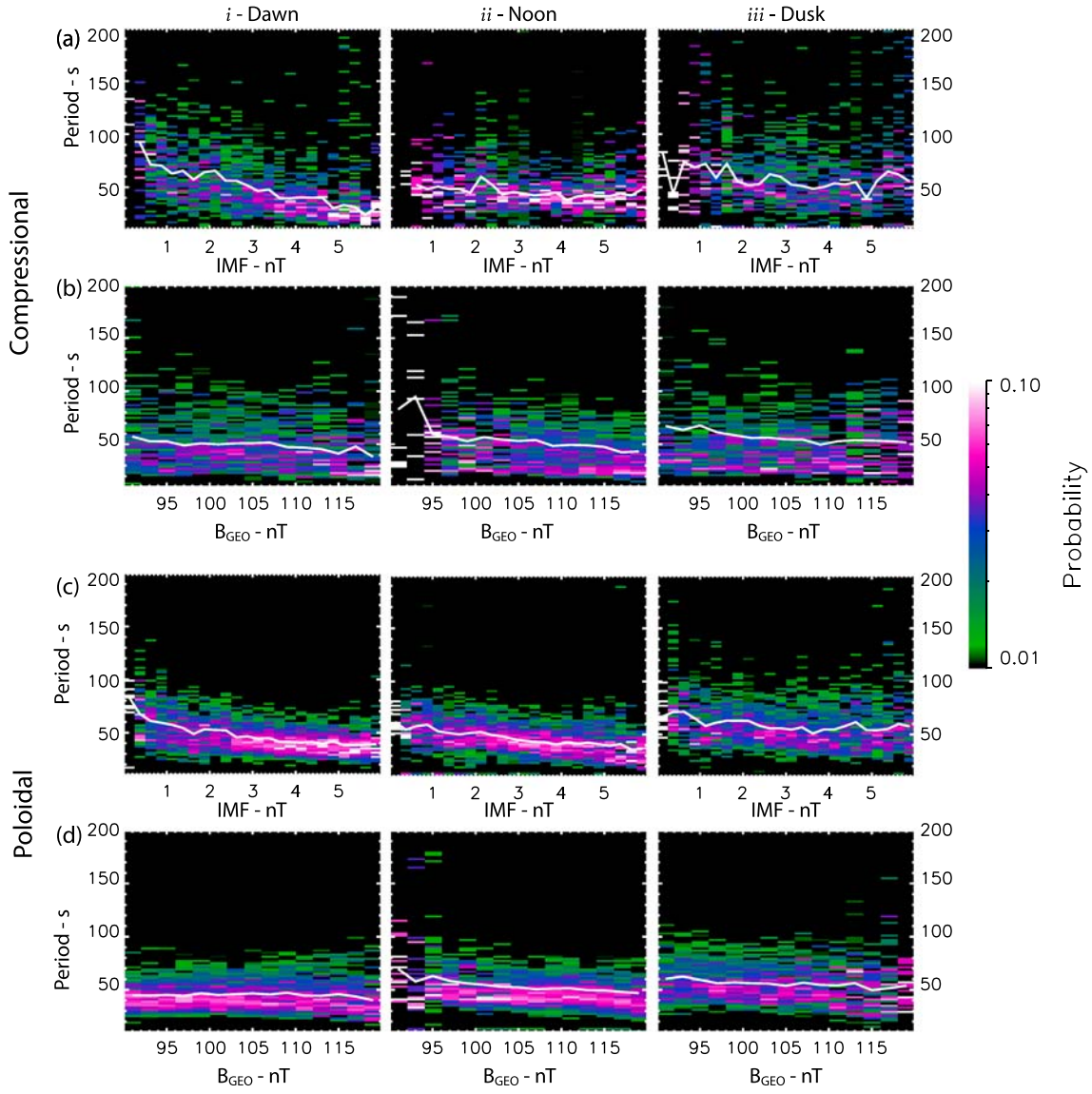

Figure 7. The probability distribution of discrete (a, b) compressional and (c, d) poloidal ULF wave periods as a function of IMF strength (a, c) and the strength of the local magnetic field observed at GOES (b, d). Columns i–iii separate the dawn, noon, and dusk MLT sectors. The white lines in each panel show the median wave period in a given IMF or local magnetic field bin. The midnight sector and toroidal waves have not been included as there is no clear relation between the observed IMF or local magnetic field strength with the period of the wave.

i and ii show the distribution and probability distribution of discrete ULF waves as a function of log period (radial axis, 10^1 to 10^3 s, 10–1,000 s) and MLT (azimuthal axis). As previously noted in section 3.1, discrete compressional and poloidal ULF wave intervals are more likely to occur in the morning and noon MLT sectors. This pattern of discrete wave activity is also apparent in Figure 6, i and ii; both the compressional and poloidal components show a preference for discrete Pc3–4 ULF wave activity (10–150 s) in the dawn and noon sectors. Discrete toroidal ULF wave intervals are confined to the postmidnight sector with periods less than 100 s, corresponding to the Pi2 band (40–150 s), a band of impulsive ULF waves associated with nightside and geomagnetic storm activity (Jacobs et al., 1964).

The probability distributions in Figure 6, ii show the probability of observing a discrete wave period as a function of MLT such that each azimuthal shell adds to 1. These distributions show the most likely MLT to observe a given period and are convenient when comparing to other studies that have shown that ULF wave generation mechanisms and wave types are generally localized in MLT as discussed in the next section. Evident in Figure 6, ii is that longer period ULF waves, >100 s, tend to be most frequently observed in the

dusk and premidnight sectors in each of the three magnetic field components. Compressional waves also show a preference for longer period waves around noon and poloidal waves in the dawn and prenoon sectors (>100 s). Shorter period waves, 10–100 s, are observed most frequently in the compressional component in the noon sector, in the poloidal component in the dawn and prenoon sectors, and in the toroidal component in the postmidnight sector.

The relationship between the dominant ULF wave period and the strength of the IMF and local magnetic field is also important as it provides insight as to whether discrete waves were generated in the solar wind or locally in the magnetosphere. For example, waves generated in the solar wind have periods inversely proportional to the strength of the IMF (e.g., Takahashi et al., 1984; Troitskaia & Bol'Shakova, 1988), whereas waves generated within the magnetosphere have periods inversely proportional to the local magnetic field strength, assuming a constant magnetospheric density (e.g., Anderson, 1994).

Figure 7 illustrates the relationship between the magnitude of the IMF as well as the local magnetic field strength at GOES 15 and the observed periods of discrete ULF waves identified by AFINO as a function of magnetic field component and MLT sector. Here we concentrate on the compressional and poloidal components and the dawn, noon, and dusk sectors. Each panel in Figure 7 shows the probability distribution of observing a given period as a function of the x axis (IMF or local magnetic field strength B_{GEO}). The white lines show the median wave period in a given bin. In the dawn and noon MLT sectors (Figure 7, i and ii) there is a clear preference for shorter period ULF waves during times of strong IMF (Figures 7a and 7c) in both the compressional and poloidal magnetic field components. However, in the dusk sector, the relationship between period and IMF is unclear or absent (Figures 7a, iii and 7c, iii). Compressional mode ULF wave periods also vary inversely with the local magnetic field strength; this is true for each of the dawn, noon, and dusk sectors (Figure 7a, i–iii). A similar inverse relation between period and local magnetic field strength is observed in poloidal waves in the noon sector (Figure 7d, ii). Neither the discrete toroidal waves nor waves occurring in the midnight MLT sector show any relation between period and the magnitude of IMF or local magnetic field strength; hence, they have not been shown.

In the next section we discuss the implications of our observations for inner magnetospheric dynamics and as well as the generation of discrete ULF wave power in the inner magnetosphere.

4. Discussion and Conclusions

We have applied the previously developed AFINO code to systematically characterize the ULF wave power spectra observed by the geosynchronous GOES spacecraft and determined the occurrence and relation of intervals of discrete and broadband power to upstream solar wind and local magnetic field conditions. All three components of the local magnetic field were analyzed to create a database of 1 hr intervals of discrete and broadband ULF wave power nominally separated into compressional, poloidal, and toroidal-dominant power based on the GOES EPN coordinate system. In summary, our analysis shows that the occurrence of discrete wave power peaks in the compressional component around noon, in the poloidal component on the dawn and dusk flanks, and in the toroidal component postmidnight. Relative to ULF wave band, discrete Pc3 (10–45 s) waves peak around noon, postdawn, and predawn in the compressional, poloidal, and toroidal components, respectively. Discrete Pc4 (45–150 s) waves peak in the noon sector, on the dawn and dusk flanks, and postmidnight in the compressional, poloidal, and toroidal components, respectively. Discrete Pc5 (150–1,000 s) waves peak on the nightside in all three magnetic field components and again around noon in the compressional and poloidal magnetic field component; there are also fewer discrete Pc5 wave events than Pc3 or Pc4. Finally, intervals of broadband ULF wave power peak on the nightside and are more abundant than discrete ULF wave activity in each of the three magnetic field components and all MLT sectors with the exception of discrete poloidal waves between 05 and 12 MLT.

Comparing the occurrence and distribution of discrete compressional, poloidal, and toroidal wave power in the Pc3–5 wave bands identified by AFINO with previous studies of ULF waves in the inner magnetosphere provides a simple way with which to validate the systematic approach to characterize ULF waves employed here. Overall there is excellent agreement between the results presented here and previous studies. Statistically the occurrence of compressional Pc3–4 waves peaks in the late morning and dayside magnetosphere (e.g., Dai et al., 2015; Heilig et al., 2007) and is likely driven by the direct propagation of ion foreshock waves and subsequent coupling of these waves to local FLRs (e.g., Eastwood et al., 2005; Hartinger et al., 2013; Heilig et al., 2007). This is consistent with the occurrence of compressional Pc3–4 waves shown in Figures 2

and 6 as well as the direct relation between the IMF and period of compressional waves shown in Figure 7, which suggests that the generation of the waves identified by AFINO is external to the magnetosphere as opposed to internal. The peak in discrete Pc4 waves near noon in the poloidal magnetic field and on the dusk flank in the compressional magnetic field is consistent with the generation of ULF waves via unstable ring current ion distributions (e.g., Baddeley et al., 2004; Ozeke & Mann, 2001; Shi et al., 2018; Southwood & Hughes, 1983). This is further supported by Figure 7, which shows a direct relation between the period of compressional ULF waves and the local magnetic field strength in the dusk and noon sectors suggesting the waves are internally generated (e.g., Ozeke & Mann, 2001) as opposed to externally generated. The noon peak in the occurrence of discrete Pc4 and Pc5 waves is consistent with the direct driving of ULF wave oscillations via buffeting of the magnetosphere by solar wind density (e.g., Kepko & Viall, 2019; Kepko et al., 2002) and density variations (e.g., Takahashi & Ukhorskiy, 2007). It is important to note that though these waves need not be confined to the dawnside, they may be easier to identify on the dawn flank where they generally have larger amplitudes as compared to those observed on the dusk flank (Sibeck, 1990, and references therein).

On the nightside there is strong evidence for discrete toroidal wave activity across the Pc3–5 wave bands. In the magnetotail, the magnetic field at geosynchronous orbit can be extremely stretched such that the GOES magnetic field is unlikely to represent, or indeed measure, neatly separated compressional, poloidal, and toroidal components of ULF waves. Hence we make no comment on the wave mode structure. Nevertheless, there is a peak in the occurrence of discrete Pc3–5 wave power on the nightside. This peak is consistent with impulsive but large-amplitude Pi1–2 (1–150 s) ULF waves (Jacobs et al., 1964) associated with substorms, the formation of the substorm current wedge, injections, dipolarizations, and tail reconnection (e.g., Keiling & Takahashi, 2011; Kepko et al., 2001; Lester et al., 1983; Murphy et al., 2011, 2013; Olson, 1999; Rae & Watt, 2016; Volwerk, 2016).

Of note in the results shown in Figures 2 and 6 is that there is no clear evidence for an enhancement in discrete Pc5 waves on the dawn and dusk flanks as would be expected with ULF waves externally driven by the KHI (Wright & Mann, 2006). Pc5 waves are confined to the noon and premidnight sector in the compressional and poloidal components and the premidnight sector in the toroidal components (Figure 6). These waves are consistent with waves driven by solar wind compressions (e.g., Kepko et al., 2002; Murphy et al., 2015) and density variations (e.g., Takahashi & Ukhorskiy, 2007), unstable ion distributions (e.g., Ozeke & Mann, 2001), and impulsive but discrete waves associated with substorms (e.g., Keiling & Takahashi, 2011; Rae & Watt, 2016; Volwerk, 2016), respectively, and as described above. The lack in longer period discrete Pc5 waves on the dawn and dusk flanks may be the result of an identification bias in the AFINO analysis, a high occurrence of discrete Pc5 wave activity on the nightside, a result of the structure of field-aligned resonances on the flanks, or a combination of all three. The implementation of AFINO here characterizes a single discrete frequency based on model S_1. Because model S_1 is fit in log-frequency space, maximizing the likelihood L is generally easier when fitting a bump at higher frequencies as there are more frequencies for the fit. Hence, in its current implementation, AFINO only identifies a single wave, and when two waves are present, the algorithm is more likely to identify the wave at higher frequency (or shorter period). In addition, the fundamental mode of toroidal FLRs has a node in magnetic field perturbation at the magnetic equator (e.g., Takahashi et al., 2015). These fundamental modes are generally associated with longer period ULF waves in the Pc5 wave band (cf. Takahashi et al., 2015). Thus the field-aligned structure and GOES-15's close proximity to the magnetic equator will make it difficult to observe toroidal mode Pc5 oscillations. Together this in part explains the abundance of poloidal mode Pc3 and Pc4 waves and lack of toroidal mode Pc5 waves. With regard to the occurrence of Pc5 wave, intervals of discrete wave activity peak on the nightside and may mask Pc5 wave activity on the dawn and dusk flanks. Figure 3c, iii does show some evidence of this as the ratio of discrete to broadband toroidal ULF wave intervals increases as v_{sw} increases as would be expected with KHI-driven waves (Mann & Wright, 1999). Despite this, the overall agreement of the distribution of discrete waves identified with AFINO and the generation mechanism inferred from the relation of the period to the IMF and local magnetic field strength with previous studies demonstrates the utility and robustness of AFINO for identifying discrete waves within the magnetosphere.

Comparing the occurrence ratio of discrete to broadband ULF wave power R_{dis} with solar wind activity, we find that in general, as solar wind activity increases, the relative occurrence of broadband wave activity also increases. With respect to solar wind velocity and density, there is an increase in broadband ULF wave intervals throughout the magnetosphere as v_{sw}, density ρ and σ_ρ increase. There are however two exceptions to this: (1) As solar wind velocity v_{sw} increases, the relative occurrence of discrete toroidal ULF waves in

the dawn and dusk sectors increases, and (2) during intervals of very high solar wind density ρ (>15), the relative occurrence in discrete ULF waves power increases throughout the dayside magnetosphere and in each of the compressional, poloidal, and toroidal magnetic field components. This increase in discrete wave activity is likely the direct driving of ULF waves by solar density variations and the coupling of the KHI instability to localized FLRs as v_{sw} increases, as discussed above.

With respect to the IMF there is an overall decrease in R_{dis} resulting from an increase in broadband and decrease in discrete waves as B_z becomes increasingly positive/negative and for cone angles around 90°. Enhanced negative B_z (and consequently cone angles near 90°) will lead to an increase in magnetopause reconnection (Lockwood et al., 1989), geomagnetic activity (e.g., O'Brien et al., 2002), and ULF wave power (Bentley et al., 2019; Murphy et al., 2015). Such is the case for geomagnetic storms that are associated with strong intervals of southward IMF (Kataoka & Miyoshi, 2006; Murphy et al., 2018). At lower cone angles, the relative occurrence of discrete wave intervals increases. Taking into account the distribution of Pc3–4 waves discussed above this increase is consistent with the generation of discrete waves by a cyclotron resonance of ions in the foreshock region (e.g., Hartinger et al., 2013). Overall, as solar wind activity increases, there is a general increase in broadband ULF wave activity throughout the magnetosphere. This may be the result of increased geomagnetic activity and several ULF wave generation mechanisms existing at the same time resulting in an increase in broadband wave power. This increase in broadband ULF wave activity has important implications for wave-particle interactions and the dynamics of the radiation belt during enhanced solar wind and geomagnetic activity.

Both the discrete and broadband intervals of ULF power identified by AFINO play a fundamental role in the dynamics of the magnetosphere. Intervals of discrete ULF wave power interact coherently with electrons via the drift (e.g., Elkington et al., 1999, 2003) and drift-bounce (e.g., Ozeke & Mann, 2008; Yeoman & Wright, 2001) resonances. Conversely, intervals of broadband wave power interact stochastically via ULF wave radial diffusion (e.g., Ozeke et al., 2013) with electrons again through the drift and drift-bounce resonances. In either the coherent or stochastic interaction the strength of the wave-particle interaction is dependent on the amplitude of the wave, though in general, the coherent interaction is stronger than the stochastic (e.g., Degeling et al., 2008; Elkington et al., 2003). Further, the ULF wave period, azimuthal wave number, and in the case of drift-bounce resonance, the field-aligned harmonic mode determines the energy of the electron with which the waves interact. For a fixed electron energy satisfying the drift and drift-bounce resonance higher azimuthal wave numbers and/or field-aligned harmonic modes requires a higher-frequency ULF wave (shorter periods). Considering a spectra of possible azimuthal wave numbers and field-aligned harmonics observed in the magnetosphere, ULF waves through the Pc3–5 wave bands can interact with electrons from hundreds of keV to multiple MeV (e.g., Murphy et al., 2018; Ozeke & Mann, 2008).

Quantifying the occurrence of broadband and discrete ULF waves in the Earth's magnetosphere is fundamental to accurately characterizing ULF wave-particle interactions. This is especially true during geomagnetic storms where the interaction between radiation belt electrons and the ULF waves is assumed to be the result of radial diffusion. The results presented here help to characterize this interaction and validate the use of radial diffusion during geomagnetic storms. The relative occurrence of discrete to broadband ULF wave power decreases during periods of high-speed solar wind v_{sw}, enhanced density ρ, and increasingly positive or negative B_z associated with geomagnetic storms (Kataoka & Miyoshi, 2006; Miyoshi et al., 2013), enhanced ULF wave activity (Bentley et al., 2019; Mathie & Mann, 2001; Murphy et al., 2015; Pahud et al., 2009; Rae et al., 2012; Takahashi & Ukhorskiy, 2007), and radiation belt dynamics (Kilpua et al., 2015; Mathie & Mann, 2000; Murphy et al., 2018). An increase in broadband ULF wave activity during increased solar wind activity and driving effectively leads to an enhancement in ULF-driven radial diffusion. During less active solar wind conditions the relative occurrence of discrete to broadband wave power tends to increase; however, the occurrence of broadband wave power almost always exceeds that of discrete wave power ($R_{dis} < 0.5$; Figures 2 and 4). Overall the results presented here indicate that discrete ULF oscillations can account for up to one third of all ULF wave activity at geosynchronous orbit, across a variety of solar wind conditions. While broadband wave power tends to dominate, discrete ULF oscillations still account for a large portion of ULF wave activity and are therefore likely to have an important influence on electrons in the outer radiation belt as wave-particle interactions with discrete ULF modes can be much more efficient than with broadband modes (e.g., Degeling et al., 2008; Elkington et al., 2003). It is important to emphasize that the results presented here are limited to geosynchronous orbit and the occurrence of discrete and broadband ULF wave intervals. Future work could expand on the results presented here to investigate

both the radial and MLT dependence of discrete and broadband ULF wave power as well as the variation in discrete and broadband wave power as function solar wind driving. Such an investigation would help to determine if the results here can be extended to lower L shells in the heart of the outer radiation belt. With regard to ULF wave modeling, a useful next step would be to model the discrete ULF (e.g., Claudepierre et al., 2008, 2009, 2010; Hartinger et al., 2014) and broadband ULF (e.g., Claudepierre et al., 2010; Ellington et al., 2016; Elsden & Wright, 2018) wave activity in the magnetosphere separately. The wave power and characteristics of the discrete ULF modes can then be used to investigate the strength of wave-particle interactions using accurate models of the ULF waves (e.g., Degeling et al., 2011; Komar et al., 2017) and quantitatively compared to radial diffusion simulations (e.g., Ozeke et al., 2013). Only once the strength of the discrete wave-particle interactions has been quantified will it be clear whether the effects of discrete ULF modes should be included in outer radiation belt diffusion models. However, the results presented here indicate that separate quantification and analysis of discrete ULF modes is now required; this is consistent with other studies that have demonstrated that diffusive processes may not be an accurate representation of the wave-particle interactions for other wave modes and that nonlinear effects may be important in, for instance, the interaction of chorus (Foster et al., 2017) and electromagnetic ion cyclotron (Albert & Bortnik, 2009) waves with radiation belt electrons.

Data Availability Statement

GOES and solar wind data are available online (https://www.ngdc.noaa.gov/stp/satellite/goes/ and https://omniweb.gsfc.nasa.gov).

Acknowledgments
K. R. M. is partially funded by the National Aeronautics and Space Administration (NASA) ROSES Guest Investigator 18-HGIO18_2-0122 and Space Weather Operations to Research 18-HSWO2R18-0010. A. R. I. acknowledges support from the Heliophysics Data Environment Emphasis program (19-HDEE19_2-0001) for continued development of the AFINO analysis code. I. J. R. is funded in part by the U.K. Science and Technology Facilities Council (STFC) Grants ST/L000563/1 and ST/N000722 and the U.K. Natural Environment Research Council (NERC) Grant NE/L007495/1. C. E. J. W. is funded in part by the U.K. STFC Grant ST/M000885/1 and NERC Grant NE/P017274/1.

References

Albert, J. M., & Bortnik, J. (2009). Nonlinear interaction of radiation belt electrons with electromagnetic ion cyclotron waves. *Geophysical Research Letters*, *36*, L12110. https://doi.org/10.1029/2009GL038904

Anderson, B. J. (1994). An overview of spacecraft observations of 10 s to 600 s period magnetic pulsations in the Earth's magnetosphere. In M. J. Engebretson, K. Takahashi, & M. Scholer (Eds.), *Solar wind sources of magnetospheric ultra-low-frequency waves, Geophysical Monograph Series* (Vol. 81, pp. 25–43). Washington, DC: American Geophysical Union. https://doi.org/10.1029/GM081p0025

Baddeley, L. J., Yeoman, T. K., Wright, D. M., Trattner, K. J., & Kellet, B. J. (2004). A statistical study of unstable particle populations in the global ring current and their relation to the generation of high *m* ULF waves, *Technical Report*.

Belcher, J. W., & Davis, L. (1971). Large-amplitude Alfvén waves in the interplanetary medium, 2. *Journal of Geophysical Research*, *76*(16), 3534–3563. https://doi.org/10.1029/JA076i016p03534

Bentley, S. N., Watt, C. E. J., Rae, I. J., Owens, M. J., Murphy, K., Lockwood, M., & Sandhu, J. K. (2019). Capturing uncertainty in magnetospheric ultralow frequency wave models. *Space Weather*, *17*, 599–618. https://doi.org/10.1029/2018SW002102

Bier, E. A., Owusu, N., Engebretson, M. J., Posch, J. L., Lessard, M. R., & Pilipenko, V. A. (2014). Investigating the IMF cone angle control of Pc3-4 pulsations observed on the ground. *Journal of Geophysical Research: Space Physics*, *119*, 1797–1813. https://doi.org/10.1002/2013JA019637

Brautigam, D. H., Ginet, G. P., Albert, J. M., Wygant, J. R., Rowland, D. E., Ling, A., & Bass, J. (2005). CRRES electric field power spectra and radial diffusion coefficients. *Journal of Geophysical Research*, *110*, A02214. https://doi.org/10.1029/2004JA010612

Broomhall, A.-M., Davenport, J. R. A., Hayes, L. A., Inglis, A. R., Kolotkov, D. Y., McLaughlin, J. A., et al. (2019). A blueprint of state-of-the-art techniques for detecting quasi-periodic pulsations in solar and stellar flares. *Astrophysical Journal Supplement Series*, *244*(2), 44. https://doi.org/10.3847/1538-4365/ab40b3

Burnham, K. P., & Anderson, D. R. (2004). Multimodel inference: Understanding AIC and BIC in model selection. *Sociological Methods & Research*, *33*(2), 261–304. https://doi.org/10.1177/0049124104268644

Cenko, S. B., Butler, N. R., Ofek, E. O., Perley, D. A., Morgan, A. N., Frail, D. A., et al. (2010). Unveiling the origin of GRB 090709A: Lack of periodicity in a reddened cosmological long-duration gamma-ray burst. *Astronomical Journal*, *140*, 224–234. https://doi.org/10.1088/0004-6256/140/1/224

Chen, C. H. K., Leung, L., Boldyrev, S., Maruca, B. A., & Bale, S. D. (2014). Ion-scale spectral break of solar wind turbulence at high and low beta. *Geophysical Research Letters*, *41*, 8081–8088. https://doi.org/10.1002/2014GL062009

Claudepierre, S. G., Elkington, S. R., & Wiltberger, M. (2008). Solar wind driving of magnetospheric ULF waves: Pulsations driven by velocity shear at the magnetopause. *Journal of Geophysical Research*, *113*, 1–16. https://doi.org/10.1029/2007JA012890

Claudepierre, S. G., Hudson, M. K., Lotko, W., Lyon, J. G., & Denton, R. E. (2010). Solar wind driving of magnetospheric ULF waves: Field line resonances driven by dynamic pressure fluctuations. *Journal of Geophysical Research*, *115*, A11202. https://doi.org/10.1029/2010JA015399

Claudepierre, S. G., Mann, I. R., Takahashi, K., Fennell, J. F., Hudson, M. K., Blake, J. B., et al. (2013). Van Allen Probes observation of localized drift resonance between poloidal mode ultra-low frequency waves and 60 keV electrons. *Geophysical Research Letters*, *40*, 4491–4497. https://doi.org/10.1002/grl.50901

Claudepierre, S. G., Wiltberger, M., Elkington, S. R., Lotko, W., & Hudson, M. K. (2009). Magnetospheric cavity modes driven by solar wind dynamic pressure fluctuations. *Geophysical Research Letters*, *36*, L13101. https://doi.org/10.1029/2009GL039045

Dai, L., Takahashi, K., Lysak, R., Wang, C., Wygant, J. R., Kletzing, C., et al. (2015). Storm time occurrence and spatial distribution of Pc4 poloidal ULF waves in the inner magnetosphere: A Van Allen Probes statistical study. *Journal of Geophysical Research: Space Physics*, *120*, 4748–4762. https://doi.org/10.1002/2015JA021134

Degeling, A. W., Ozeke, L. G., Rankin, R., Mann, I. R., & Kabin, K. (2008). Drift resonant generation of peaked relativistic electron distributions by Pc 5 ULF waves. *Journal of Geophysical Research*, *113*, 1–10. https://doi.org/10.1029/2007JA012411

Degeling, A. W., Rankin, R., & Elkington, S. R. (2011). Convective and diffusive ULF wave driven radiation belt electron transport. *Journal of Geophysical Research*, *116*, A12217. https://doi.org/10.1029/2011JA016896

Eastwood, J. P., Lucek, E. A., Mazelle, C., Meziane, K., Narita, Y., Pickett, J., & Treumann, R. A. (2005). The foreshock. *Space Science Reviews*, *118*(1–4), 41–94. https://doi.org/10.1007/s11214-005-3824-3

Elkington, S. R. (2006). A review of ULF interactions with radiation belt electrons. In *Magnetospheric ULF waves: Synthesis and new directions* (Vol. 169, pp. 177–193). https://doi.org/10.1029/169GM12

Elkington, S. R., Hudson, M. K., & Chan, A. A. (1999). Acceleration of relativistic electrons via drift-resonant interaction with toroidal-mode Pc-5 ULF oscillations. *Geophysical Research Letters*, *26*(21), 3273–3276. https://doi.org/10.1029/1999GL003659

Elkington, S. R., Hudson, M. K., & Chan, A. A. (2003). Resonant acceleration and diffusion of outer zone electrons in an asymmetric geomagnetic field. *Journal of Geophysical Research*, *108*(A3). https://doi.org/10.1029/2001JA009202

Ellington, S. M., Moldwin, M. B., & Liemohn, M. W. (2016). Local time asymmetries and toroidal field line resonances: Global magnetospheric modeling in SWMF. *Journal of Geophysical Research: Space Physics*, *121*, 2033–2045. https://doi.org/10.1002/2015JA021920

Elsden, T., & Wright, A. N. (2018). The broadband excitation of 3-D Alfvén resonances in a MHD waveguide. *Journal of Geophysical Research: Space Physics*, *123*, 530–547. https://doi.org/10.1002/2017JA025018

Fei, Y., Chan, A. A., Elkington, S. R., & Wiltberger, M. J. (2006). Radial diffusion and MHD particle simulations of relativistic electron transport by ULF waves in the September 1998 storm. *Journal of Geophysical Research*, *111*, A12209. https://doi.org/10.1029/2005JA011211

Foster, J. C., Erickson, P. J., Omura, Y., Baker, D. N., Kletzing, C. A., & Claudepierre, S. G. (2017). Van Allen Probes observations of prompt MeV radiation belt electron acceleration in nonlinear interactions with VLF chorus. *Journal of Geophysical Research: Space Physics*, *122*, 324–339. https://doi.org/10.1002/2016JA023429

Gruber, D., Lachowicz, P., Bissaldi, E., Briggs, M. S., Connaughton, V., Greiner, J., et al. (2011). Quasi-periodic pulsations in solar flares: New clues from the Fermi Gamma-Ray Burst Monitor. *Astronomy and Astrophysics*, *533*, A61. https://doi.org/10.1051/0004-6361/201117077

Hartinger, M. D., Moldwin, M. B., Zou, S., Bonnell, J. W., & Angelopoulos, V. (2015). ULF wave electromagnetic energy flux into the ionosphere: Joule heating implications. *Journal of Geophysical Research: Space Physics*, *120*, 494–510. https://doi.org/10.1002/2014JA020129

Hartinger, M. D., Turner, D. L., Plaschke, F., Angelopoulos, V., & Singer, H. (2013). The role of transient ion foreshock phenomena in driving Pc5 ULF wave activity. *Journal of Geophysical Research: Space Physics*, *118*, 299–312. https://doi.org/10.1029/2012JA018349

Hartinger, M. D., Welling, D., Viall, N. M., Moldwin, M. B., & Ridley, A. (2014). The effect of magnetopause motion on fast mode resonance. *Journal of Geophysical Research: Space Physics*, *119*, 8212–8227. https://doi.org/10.1002/2014JA020401

Hasegawa, A., Tsui, K. H., & Assis, A. S. (1983). A theory of long period magnetic pulsations, 3. Local field line oscillations. *Geophysical Research Letters*, *10*(8), 765–767. https://doi.org/10.1029/GL010i008p00765

Heilig, B., Lühr, H., & Rother, M. (2007). Comprehensive study of ULF upstream waves observed in the topside ionosphere by CHAMP and on the ground. *Annales Geophysicae*, *25*(3), 737–754. https://doi.org/10.5194/angeo-25-737-2007

Horne, R. B., & Thorne, R. M. (1998). Potential waves for relativistic electron scattering and stochastic acceleration during magnetic storms. *Geophysical Research Letters*, *25*(15), 3011–3014. https://doi.org/10.1029/98GL01002

Hughes, W. J. (1974). The effect of the atmosphere and ionosphere on long period magnetospheric micropulsations. *Planetary and Space Science*, *22*(8), 1157–1172. https://doi.org/10.1016/0032-0633(74)90001-4

Huppenkothen, D., Bachetti, M., Stevens, A. L., Migliari, S., Balm, P., Hammad, O., et al. (2019). Stingray: A modern Python library for spectral timing. *Astrophysical Journal*, *881*(1), 39. https://doi.org/10.3847/1538-4357/ab258d

Huppenkothen, D., Watts, A. L., Uttley, P., van der Horst, A. J., van der Klis, M., Kouveliotou, C., et al. (2013). Quasi-periodic oscillations and broadband variability in short magnetar bursts. *Astrophysical Journal*, *768*, 87. https://doi.org/10.1088/0004-637X/768/1/87

Inglis, A. R., Ireland, J., Dennis, B. R., Hayes, L., & Gallagher, P. (2016). A large-scale search for evidence of quasi-periodic pulsations in solar flares. *Astrophysical Journal*, *833*, 284. https://doi.org/10.3847/1538-4357/833/2/284

Inglis, A. R., Ireland, J., & Dominique, M. (2015). Quasi-periodic pulsations in solar and stellar flares: Re-evaluating their nature in the context of power-law flare Fourier spectra. *Astrophysical Journal*, *798*, 108. https://doi.org/10.1088/0004-637X/798/2/108

Ireland, J., McAteer, R. T. J., & Inglis, A. R. (2015). Coronal Fourier power spectra: Implications for coronal seismology and coronal heating. *Astrophysical Journal*, *798*, 1. https://doi.org/10.1088/0004-637X/798/1/1

Jacobs, J. A., Kato, Y., Matsushita, S., & Troitskaya, V. A. (1964). Classification of geomagnetic micropulsations. *Journal of Geophysical Research*, *69*(1). https://doi.org/10.1029/JZ069i001p00180

Kataoka, R., & Miyoshi, Y. (2006). Flux enhancement of radiation belt electrons during geomagnetic storms driven by coronal mass ejections and corotating interaction regions. *Space Weather*, *4*(9), 1–11. https://doi.org/10.1029/2005SW000211

Keiling, A., & Takahashi, K. (2011). Review of Pi2 models. https://doi.org/10.1007/s11214-011-9818-4

Kepko, L., Kivelson, M. G., & Yumoto, K. (2001). Flow bursts, braking, and Pi2 pulsations. *Journal of Geophysical Research*, *106*(A2), 1903. https://doi.org/10.1029/2000JA000158

Kepko, L., Spence, H. E., & Singer, H. J. (2002). ULF waves in the solar wind as direct drivers of magnetospheric pulsations. *Geophysical Research Letters*, *29*(8), 1197. https://doi.org/10.1029/2001GL014405

Kepko, L., & Viall, N. M. (2019). The source, significance, and magnetospheric impact of periodic density structures within stream interaction regions. *Journal of Geophysical Research: Space Physics*, *124*, 7722–7743. https://doi.org/10.1029/2019ja026962

Kilpua, E. K. J., Hietala, H., Turner, D. L., Koskinen, H. E. J., Pulkkinen, T. I., Rodriguez, J. V., et al. (2015). Unraveling the drivers of the storm-time radiation belt response. *Geophysical Research Letters*, *42*, 3076–3084. https://doi.org/10.1002/2015GL063542

King, J. H., & Papitashvili, N. E. (2005). Solar wind spatial scales in and comparisons of hourly Wind and ACE plasma and magnetic field data. *Journal of Geophysical Research*, *110*, A02104. https://doi.org/10.1029/2004JA010649

Kivelson, M. G. (2006). ULF waves from the ionosphere to the outer planets. In Takahashi, K., Chi, P. J., Denton, R. E., & Lysak, R. L. (Eds.), *Magnetospheric ULF waves: Synthesis and new directions* (pp. 11–30). https://doi.org/10.1029/169GM04

Komar, C. M., Glocer, A., Hartinger, M. D., Murphy, K. R., Fok, M. C., & Kang, S. B. (2017). Electron drift resonance in the MHD-coupled comprehensive inner magnetosphere-ionosphere model. *Journal of Geophysical Research: Space Physics*, *122*, 12,006–12,018. https://doi.org/10.1002/2017JA024163

Lepping, R. P., Acũna, M. H., Burlaga, L. F., Farrell, W. M., Slavin, J. A., Schatten, K. H., et al. (1995). The wind magnetic field investigation. *Space Science Reviews*, *71*, 207–229. https://doi.org/10.1007/BF00751330

Lester, M., Hughes, J. W., & Singer, H. J. (1983). Polarization patterns of Pi 2 magnetic pulsations and the substorm current wedge. *Journal of Geophysical Research*, *88*(A10), 7958. https://doi.org/10.1029/JA088iA10p07958

Lockwood, M., Sandholt, P. E., Cowley, S. W. H., & Oguti, T. (1989). Interplanetary magnetic field control of dayside auroral activity and the transfer of momentum across the dayside magnetopause. *Planetary and Space Science*, *37*(11), 1347–1365. https://doi.org/10.1016/0032-0633(89)90106-2

Mann, I. R., Lee, E. A., Claudepierre, S. G., Fennell, J. F., Degeling, A., Rae, I. J., et al. (2013). Discovery of the action of a geophysical synchrotron in the Earth's Van Allen radiation belts. *Nature Communications*, *4*, 1–6. https://doi.org/10.1038/ncomms3795

Mann, I. R., Voronkov, I., Dunlop, M., Donovan, E., Yeoman, T. K., Milling, D. K., et al. (2002). Coordinated ground-based and Cluster observations of large amplitude global magnetospheric oscillations during a fast solar wind speed interval. *Annales Geophysicae*, *20*(4), 405–426. https://doi.org/10.5194/angeo-20-405-2002

Mann, I. R., & Wright, A. N. (1999). Diagnosing the excitation mechanisms of Pc5 magnetospheric flank waveguide modes and FLRs. *Geophysical Research Letters*, *26*(16), 2609–2612. https://doi.org/10.1029/1999GL900573

Mathie, R. A., & Mann, I. R. (2000). A correlation between extended intervals of ULF wave power and storm-time geosynchronous relativistic electron flux enhancements. *Geophysical Research Letters*, *27*(20), 3261–3264. https://doi.org/10.1029/2000GL003822

Mathie, R., & Mann, I. R. (2001). On the solar wind control of Pc5 ULF pulsation power at mid-latitudes: Implications for MeV electron acceleration in the outer radiation belt. *Journal of Geophysical Research*, *106*, 29,783–29,796. https://doi.org/10.1029/2001JA000002

Mauk, B. H., Fox, N. J., Kanekal, S. G., Kessel, R. L., Sibeck, D. G., & Ukhorskiy (2013). Science objectives and rationale for the Radiation Belt Storm Probes mission. *Space Science Reviews*, *179*(1–4), 3–27. https://doi.org/10.1007/s11214-012-9908-y

Menk, F. W. (2011). Magnetospheric ULF waves: A review. https://doi.org/10.1007/978-94-007-0501-2_13

Menk, F. W., & Waters, C. L. (2013). *Magnetoseismology*. Weinheim, Germany: Wiley-VCH Verlag GmbH & Co. KGaA. https://doi.org/10.1002/9783527652051

Mills, K. J., & Wright, A. N. (1999). Azimuthal phase speeds of field line resonances driven by Kelvin-Helmholtz unstable waveguide modes. *Journal of Geophysical Research*, *104*, 22,667–22,678. https://doi.org/10.1029/1999JA900280

Miyoshi, Y., Kataoka, R., Kasahara, Y., Kumamoto, A., Nagai, T., & Thomsen, M. F. (2013). High-speed solar wind with southward interplanetary magnetic field causes relativistic electron flux enhancement of the outer radiation belt via enhanced condition of whistler waves. *Geophysical Research Letters*, *40*, 4520–4525. https://doi.org/10.1002/grl.50916

Murphy, K. R., Inglis, A. R., Sibeck, D. G., Rae, I. J., Watt, C. E. J., Silveira, M., et al. (2018). Determining the mode, frequency, and azimuthal wave number of ULF waves during a HSS and moderate geomagnetic storm. *Journal of Geophysical Research: Space Physics*, *123*, 6457–6477. https://doi.org/10.1029/2017JA024877

Murphy, K. R., Mann, I. R., Jonathan Rae, I., & Milling, D. K. (2011). Dependence of ground-based Pc5 ULF wave power on F10.7 solar radio flux and solar cycle phase. *Journal of Atmospheric and Solar-Terrestrial Physics*, *73*(11–12), 1500–1510. https://doi.org/10.1016/j.jastp.2011.02.018

Murphy, K. R., Mann, I. R., Rae, I. J., Waters, C. L., Frey, H. U., Kale, A., et al. (2013). The detailed spatial structure of field-aligned currents comprising the substorm current wedge. *Journal of Geophysical Research: Space Physics*, *118*, 7714–7727. https://doi.org/10.1002/2013JA018979

Murphy, K. R., Mann, I. R., & Sibeck, D. G. (2015). On the dependence of storm-time ULF wave power on magnetopause location: Impacts for ULF wave radial diffusion. *Geophysical Research Letters*, *42*, 9676–9684. https://doi.org/10.1002/2015GL066592

Murphy, K. R., Mann, I. R., Sibeck, D. G., Rae, I. J., Watt, C. E. J., Ozeke, L. G., et al. (2020). A framework for understanding and quantifying the loss and acceleration of relativistic electrons in the outer radiation belt during geomagnetic storms. *Space Weather*, *18*, e2020SW002477. https://doi.org/10.1029/2020SW002477

Nita, GeluM., Fleishman, G. D., Gary, D. E., Marin, W., & Boone, K. (2014). Fitting FFT-derived spectra: Theory, tool, and application to solar radio spike decomposition. *Astrophysical Journal*, *789*(2), 152. https://doi.org/10.1088/0004-637X/789/2/152

O'Brien, T. P., McPherron, R. L., Sornette, D., Reeves, G. D., Friedel, R., & Singer, H. J. (2001). Which magnetic storms produce relativistic electrons at geosynchronous orbit? *Journal of Geophysical Research*, *106*(A8), 15,533. https://doi.org/10.1029/2001JA000052

O'Brien, T. P., Thompson, S. M., & McPherron, R. L. (2002). Steady magnetospheric convection: Statistical signatures in the solar wind and *AE*. *Geophysical Research Letters*, *29*(7), 1130. https://doi.org/10.1029/2001GL014641

Olifer, L., Mann, I. R., Ozeke, L. G., Rae, I. J., & Morley, S. K. (2019). On the relative strength of electric and magnetic ULF wave radial diffusion during the March 2015 geomagnetic storm. *Journal of Geophysical Research: Space Physics*, *124*, 2569–2587. https://doi.org/10.1029/2018JA026348

Olson, J. V. (1999). Pi2 pulsations and substorm onsets: A review. *Journal of Geophysical Research*, *104*(A8), 17,499. https://doi.org/10.1029/1999JA900086

Ozeke, L. G., & Mann, I. R. (2001). Modeling the properties of high-*m* Alfvén waves driven by the drift-bounce resonance mechanism. *Journal of Geophysical Research*, *106*(A8), 15,583. https://doi.org/10.1029/2000JA000393

Ozeke, L. G., & Mann, I. R. (2008). Energization of radiation belt electrons by ring current ion driven ULF waves. *Journal of Geophysical Research*, *113*, A02201. https://doi.org/10.1029/2007JA012468

Ozeke, L. G., Mann, I. R., Murphy, K. R., Jonathan Rae, I., & Milling, D. K. (2014). Analytic expressions for ULF wave radiation belt radial diffusion coefficients. *Journal of Geophysical Research: Space Physics*, *119*, 1587–1605. https://doi.org/10.1002/2013JA019204

Ozeke, L. G., Mann, I. R., Murphy, K. R., Rae, I. J., & Chan, A. (2013). ULF wave-driven radial diffusion simulations of the outer radiation belt, *Geophysical monograph series* (vol. 199, pp. 139–150). https://doi.org/10.1029/2012GM001332

Pahud, D. M., Rae, I. J., Mann, I. R., Murphy, K. R., & Amalraj, V. (2009). Ground-based Pc5 ULF wave power: Solar wind speed and MLT dependence. *Journal of Atmospheric and Solar-Terrestrial Physics*, *71*(10–11), 1082–1092. https://doi.org/10.1016/j.jastp.2008.12.004

Plaschke, F. (2016). ULF waves at the magnetopause. In A. Keiling, D.-H. Lee, & V. Nakariakov (Eds.), *Low-frequency waves in space plasmas* (pp. 193–212).

Rae, I. J., Donovan, E. F., Mann, I. R., Fenrich, F. R., Watt, C. E. J., Milling, D. K., et al. (2005). Evolution and characteristics of global Pc5 ULF waves during a high solar wind speed interval. *Journal of Geophysical Research*, *110*, A12211. https://doi.org/10.1029/2005ja011007

Rae, I. J., Mann, I. R., Murphy, K. R., Ozeke, L. G., Milling, D. K., Chan, A. A., et al. (2012). Ground-based magnetometer determination of in situ Pc4–5 ULF electric field wave spectra as a function of solar wind speed. *Journal of Geophysical Research*, *117*, A04221. https://doi.org/10.1029/2011JA017335

Rae, I. J., & Watt, C. E. J. (2016). ULF waves above the nightside auroral oval during substorm onset. In A. Keiling, D.-H. Lee, & V. Nakariakov (Eds.), *Low-Frequency Waves in Space Plasmas* (pp. 99–120).

Raftery, A. E. (1995). Bayesian model selection in social research. *Sociological Methodology*, *25*, 111–163.

Sarris, T. E. (2014). Estimates of the power per mode number of broadband ULF waves at geosynchronous orbit. *Journal of Geophysical Research: Space Physics*, *119*, 5539–5550. https://doi.org/10.1002/2013JA019238

Schulz, M., & Lanzerotti, L. J. (1974). Particle diffusion in the radiation belts. *Physics and Chemistry in Space*, *7*. https://doi.org/10.1007/978-3-642-65675-0

Schwarz, G. (1978). Estimating the dimension of a model. *Annals of Statistics*, *6*(2), 461–464.
Shi, X., Baker, J. B. H., Ruohoniemi, J. M., Hartinger, M. D., Murphy, K. R., Rodriguez, J. V., et al. (2018). Long-lasting poloidal ULF waves observed by multiple satellites and high-latitude SuperDARN radars. *Journal of Geophysical Research: Space Physics*, *123*, 8422–8438. https://doi.org/10.1029/2018JA026003
Sibeck, D. G. (1990). A model for the transient magnetospheric response to sudden solar wind dynamic pressure variations. *Journal of Geophysical Research*, *95*(A4), 3755–3771. https://doi.org/10.1029/JA095iA04p03755
Singer, H., Matheson, L., Grubb, R., Newman, A., & Bouwer, D. (1996). Monitoring space weather with the GOES magnetometers. In E. R. Washwell (Ed.), *GOES-8 and beyond* (Vol. 2812, pp. 299–308). Denver, CO, United States: SPIE. https://doi.org/10.1117/12.254077
Smith, E. J., Balogh, A., Neugebauer, M., & McComas, D. (1995). Ulysses observations of Alfvén waves in the southern and northern solar hemispheres. *Geophysical Research Letters*, *22*(23), 3381–3384. https://doi.org/10.1029/95GL03268
Southwood, D. J. (1968). The hydromagnetic stability of the magnetospheric boundary. *Planetary and Space Science*, *16*, 587–605. https://doi.org/10.1016/0032-0633(68)90100-1
Southwood, D. J., Dungey, J. W., & Etherington, R. J. (1969). Bounce resonant interaction between pulsations and trapped particles. *Planetary and Space Science*, *17*(3), 349–361. https://doi.org/10.1016/0032-0633(69)90068-3
Southwood, D. J., & Hughes, W. J. (1983). Theory of hydromagnetic waves in the magnetosphere. *Space Science Reviews*, *35*(4), 301–366. https://doi.org/10.1007/BF00169231
Stewart, B. (1861). On the great magnetic disturbance which extended from August 28 to September 7, 1859, as recorded by photography at the Kew Observatory. *Philosophical Transactions of the Royal Society of London*, *151*, 423–430.
Stone, E. C., Frandsen, A. M., Mewaldt, R. A., Christian, E. R., Margolies, D., Ormes, J. F., & Snow, F. (1998). The Advanced Composition Explorer. *Space Science Reviews*, *86*, 1–22. https://doi.org/10.1023/A:1005082526237
Takahashi, K. (2016). ULF waves in the inner magnetosphere. In A. Keiling, D.-H. Lee, & V. Nakariakov (Eds.), *Low-frequency waves in space plasmas* (pp. 51–63). https://doi.org/10.1002/9781119055006.ch4
Takahashi, K., & Denton, R. E. (2007). Magnetospheric seismology using multiharmonic toroidal waves observed at geosynchronous orbit. *Journal of Geophysical Research*, *112*, A05204. https://doi.org/10.1029/2006JA011709
Takahashi, K., Hartinger, M. D., Angelopoulos, V., & Glassmeier, K.-H. (2015). A statistical study of fundamental toroidal mode standing Alfvén waves using THEMIS ion bulk velocity data. *Journal of Geophysical Research: Space Physics*, *120*, 6474–6495. https://doi.org/10.1002/2015JA021207
Takahashi, K., & McPherron, R. L. (1982). Harmonic structure of Pc 3–4 pulsations. *Journal of Geophysical Research*, *87*(A3), 1504–1516. https://doi.org/10.1029/JA087iA03p01504
Takahashi, K., & McPherron, R. L. (1984). Standing hydromagnetic oscillations in the magnetosphere. *Planetary and Space Science*, *32*(11), 1343–1359. https://doi.org/10.1016/0032-0633(84)90078-3
Takahashi, K., McPherron, R. L., & Terasawa, T. (1984). Dependence of the spectrum of Pc 3–4 pulsations on the interplanetary magnetic field. *Journal of Geophysical Research*, *89*(A5), 2770–2780. https://doi.org/10.1029/JA089iA05p02770
Takahashi, K., & Ukhorskiy, A. Y. (2007). Solar wind control of Pc5 pulsation power at geosynchronous orbit. *Journal of Geophysical Research*, *112*, A11205. https://doi.org/10.1029/2007JA012483
Thorne, R. M. (2010). Radiation belt dynamics: The importance of wave-particle interactions. *Geophysical Research Letters*, *37*(22), 1–7. https://doi.org/10.1029/2010GL044990
Troitskaia, V. A., & Bol'Shakova, O. V. (1988). Diagnostics of the magnetosphere using multipoint measurements of ULF-waves. *Advances in Space Research*, *8*(9-10), 413–425. https://doi.org/10.1016/0273-1177(88)90155-X
Tsurutani, B. T., Ho, C. M., Smith, E. J., Neugebauer, M., Goldstein, B. E., Mok, J. S., et al. (1994). The relationship between interplanetary discontinuities and Alfvén waves: Ulysses observations. *Geophysical Research Letters*, *21*(21), 2267–2270. https://doi.org/10.1029/94GL02194
Vaughan, S. (2005). A simple test for periodic signals in red noise. *Astronomy and Astrophysics*, *431*, 391–403. https://doi.org/10.1051/0004-6361:20041453
Volwerk, M. (2016). ULF wave modes in the Earth's magnetotail. In A. Keiling, D.-H. Lee, & V. Nakariakov (Eds.), *Low-frequency waves in space plasmas* (pp. 139–160). https://doi.org/10.1002/9781119055006.ch9
Wharton, S. J., Wright, D. M., Yeoman, T. K., James, M. K., & Sandhu, J. K. (2019). The variation of resonating magnetospheric field lines with changing geomagnetic and solar wind conditions. *Journal of Geophysical Research: Space Physics*, *124*, 5353–5375. https://doi.org/10.1029/2019JA026848
Wright, A. N., & Mann, I. R. (2006). Global MHD eigenmodes of the outer magnetosphere. In *Magnetospheric ULF waves: Synthesis and new directions* (Vol. 169, pp. 51–72). https://doi.org/10.1029/169GM06
Yeoman, T. K., & Wright, D. M. (2001). ULF waves with drift resonance and drift-bounce resonance energy sources as observed in artificially-induced HF radar backscatter, *Technical Report*.